



**HAL**  
open science

## Numerical simulation of a thermally driven hydrogen compressor as a performance optimization tool

Vincent Nicolas, G Sdanghi, K Mozet, S Schaefer, Gaël Maranzana, A Celzard, Vanessa Fierro

► **To cite this version:**

Vincent Nicolas, G Sdanghi, K Mozet, S Schaefer, Gaël Maranzana, et al.. Numerical simulation of a thermally driven hydrogen compressor as a performance optimization tool. Applied Energy, 2022, 10.1016/j.apenergy.2022.119628 . hal-03849414

**HAL Id: hal-03849414**

**<https://hal.univ-lorraine.fr/hal-03849414v1>**

Submitted on 11 Nov 2022

**HAL** is a multi-disciplinary open access archive for the deposit and dissemination of scientific research documents, whether they are published or not. The documents may come from teaching and research institutions in France or abroad, or from public or private research centers.

L'archive ouverte pluridisciplinaire **HAL**, est destinée au dépôt et à la diffusion de documents scientifiques de niveau recherche, publiés ou non, émanant des établissements d'enseignement et de recherche français ou étrangers, des laboratoires publics ou privés.



Distributed under a Creative Commons Attribution - NonCommercial - NoDerivatives 4.0 International License

# **Numerical simulation of a thermally driven hydrogen compressor as a performance optimization tool**

V. Nicolas<sup>a\*</sup>, G. Sdanghi<sup>a,b</sup>, K. Mozet<sup>b</sup>, S. Schaefer<sup>a</sup>, G. Maranzana<sup>b</sup>,

A. Celzard<sup>a</sup>, V. Fierro<sup>a\*</sup>

<sup>a</sup> Université de Lorraine, CNRS, IJL, F-88000 Epinal, France

<sup>b</sup> Université de Lorraine, CNRS, LEMTA, F-54000 Nancy, France

---

Corresponding Author: [vincent.nicolas@univ-lorraine.fr](mailto:vincent.nicolas@univ-lorraine.fr)

[vanessa.fierro@univ-lorraine.fr](mailto:vanessa.fierro@univ-lorraine.fr)

## **Abstract**

For the first time, a thermal study and optimization of a thermally driven hydrogen compressor has been performed. Experiments on this compressor, which is a proof of concept we developed, are time-consuming, making it difficult to know the behavior of the compressor under a variety of possible thermal conditions. In order to understand its behavior, we developed a numerical model to study the evolution of hydrogen pressure, flow rate, and temperature when heat transfers are intensified by changing the heating power, the setpoint temperature, or the convective regime. Hydrogen compression and discharge were simulated by finite elements and the tank was modeled by an axisymmetric 2D geometry. The heat and mass conservation equations for hydrogen were solved and the predictions were validated by using three heating powers during desorption: 100W, 200W and 300W. A parametric numerical study on the effect of heating power and final set temperature showed that the higher the power, the more hydrogen is discharged, and that the amount of hydrogen discharged varies quasi-linearly with the final set temperature, as long as it is below 500K. Finally, we have shown that increasing the heat transfer by convection with the outside air reduces the time to reach the room temperature by approximately 75%.

**Keywords:** Numerical simulation; hydrogen; activated carbon; thermal compressor

## 1. Introduction

Although hydrogen is considered as a promising candidate to replace fossil fuels, especially in the transportation sector, its low volumetric energy density still remains a major drawback ( $0.01079 \text{ MJ L}^{-1}$  at standard temperature and pressure). Several methods are used to increase the latter value, and the most widely used is compression. High-pressure tanks of 70 MPa allow storing 6 wt.% of hydrogen considering the whole storage system, but compression requires 15% of the hydrogen lower heating value (LHV). Alternatively, a hydrogen capacity of up to 7 wt.% can be achieved by liquid storage, but hydrogen liquefaction requires about 40% of the hydrogen's LHV, and a high degree of adiabaticity of the storage tanks is almost mandatory due to the very low temperatures [1]. Magnesium-based hydrides, such as  $\text{MgH}_2$ , also allow storing 7 wt.% of hydrogen [2], but metal hydrides are relatively heavy, thus the weight ratio of stored hydrogen to the total storage system can be as low as 1-3% [3]. Moreover, very high temperatures ( $> 620 \text{ K}$ ) are required for hydrogen desorption, and the reaction enthalpy is almost 30% of the hydrogen's LHV [4].

To date, there are several hydrogen compressor technologies, which can be grouped into two categories: (i) mechanical compressors, which can be driven by either a piston or a diaphragm; (ii) non-mechanical compressors, *i.e.*, electrochemical and thermally driven compressors. A detailed description of each technology is presented elsewhere [5]. In our previous study [6], we proved that it is possible to compress hydrogen up to 70 MPa in one single stage by controlling the cyclic adsorption/desorption of hydrogen on activated carbons (ACs).

The advantage of compression by physisorption on ACs compared to compression by absorption in hydrides is the low energy of sorption (about  $6 \text{ kJ mol}_{\text{H}_2}^{-1}$  for ACs versus ten times more for absorption in hydrides) and its reversible character. The flow rate produced by these thermally driven hydrogen compressors is limited by heat transfers. A low enthalpy of sorption is an advantage in two ways: it allows to accelerate the heat transfers, thus increasing

the flow rate, and to decrease the amount of heat to be exchanged, thus increasing the energy efficiency. The experimental device presented in the following section is a proof of concept whose role is to determine the performance in terms of maximum compression pressure. It was not designed to be energy-efficient. The mass of the tank is much larger than the mass of AC it contains and frigories are lost during heating, so liquid nitrogen consumption is very important here. An optimized system would have internal heat exchangers, insulation between the AC bed and the thick wall, and at least two tanks operating in phase opposition to recover frigories from the warming tank to cool the cooling tank. In the ideal case of a perfectly insulated system, the only heat dissipation is the enthalpy of sorption that must be removed at the temperature of liquid nitrogen. The minimal energy cost of this technology is therefore the energy required to evacuate  $6 \text{ kJ mol}_{\text{H}_2}^{-1}$  at 77K. If the cold is produced by a Carnot machine operating between room temperature and 77K, with an efficiency of 35%, the ideal energy cost of compression is therefore  $17 \text{ kJ mol}_{\text{H}_2}^{-1}$  to compress hydrogen from 8MPa to 70MPa, i.e., 6% of the LHV of hydrogen, or 3 times the energy required for the same isothermal compression at room temperature. The ideal efficiency of this compressor is therefore 33% compared to isothermal compression at room temperature. Beyond the energy aspect, the advantage of this compressor, which can increase the pressure from 80 to 700 bar in a single stage, is its low capital expenditure, the absence of vibrations (no moving parts), its reliability and its life span.

Specifically, hydrogen was compressed from 8 to 70 MPa using a 0.5 L high-pressure tank filled with 0.135 kg of AC. The tank was heated from 77 to approximately 323 K to drive hydrogen desorption. A 2D-axisymmetric numerical model was also developed to describe the behavior of the adsorption/desorption compressor, and was in good agreement with the experimental data obtained. An empirical equation was also proposed to reproduce the time evolution of the 70 MPa hydrogen discharge flow. As far as we know, the adsorption/desorption compressor is a rather new technology, and very few studies have been carried out about it until

now. Richard et al. [7] obtained preliminary results on hydrogen compression in a carbon-based system by introducing hydrogen at room temperature in a tank filled with AC initially at 77 K and 0.14 MPa. The consequent increase in temperature caused the hydrogen pressure to rise to a value of about 5 MPa. The numerical investigation carried out by Sdanghi et al. [8] showed that hydrogen can be compressed from 40 to 70 MPa in an adsorption/desorption compressor using 0.25 kg of AC and heating the system from 77 to 300 K. Moreover, the authors found that the density of hydrogen in the adsorbed phase gradually increases during the charging phase to  $66 \text{ kg m}^{-3}$ , which is slightly lower than the density of liquid hydrogen, *i.e.*,  $70.8 \text{ kg m}^{-3}$ . Other numerical studies on mass and heat transfer of hydrogen in a tank filled with AC during both the charging and discharging processes can also be found in the literature, but the thermally driven hydrogen compression in such a system has not been considered there [9–14].

The system developed here has only been studied for one thermal configuration. Indeed, only a few experimental studies have been performed so far, and each of them is highly time-consuming. This experimental limitation leads to a lack of knowledge about the behavior of the compressor under other conditions, which may be an obstacle to the large-scale development of the process. Therefore, we propose to study the system under several thermal conditions, varying the heating power, setpoint temperature and convective regime, in order to understand its behavior when heat transfers are intensified using the numerical model.

In the present study, we have performed a thorough numerical investigation (2D-axisymmetric model) of the hydrogen adsorption/desorption compressor previously developed. The model used is an evolution of the one developed in our previous work [6]. Indeed, we have considered here the impact of the density of the adsorbed hydrogen phase on the compressor performance. The main objective of this study is to understand the thermal behavior of the compressor through simulations. Thus, in order to use the model and extrapolate some configurations, the model is validated under several thermal configurations by imposing for the

first time three constant powers on the heating belt (100, 200 and 300 W). The simulated evolutions are analyzed for these three scenarios in order to understand the compressor operation. In addition, a parametric study on specific parameters is carried out. Finally, the impact of temperature and heat exchange with the external environment is simulated, which can be useful to study the energy optimization of such a system.

## 2. Experimental and methods

### 2.1. Description of the adsorption-desorption compressor

We considered a system consisting in a tank filled with AC, in which the heating was carried out in two stages (Figure 1): stage #1, from 77 K to room temperature, where the heating occurs by convection with air; and stage #2, where the heating is driven by thermal resistors with constant power (100, 200 or 300 W).

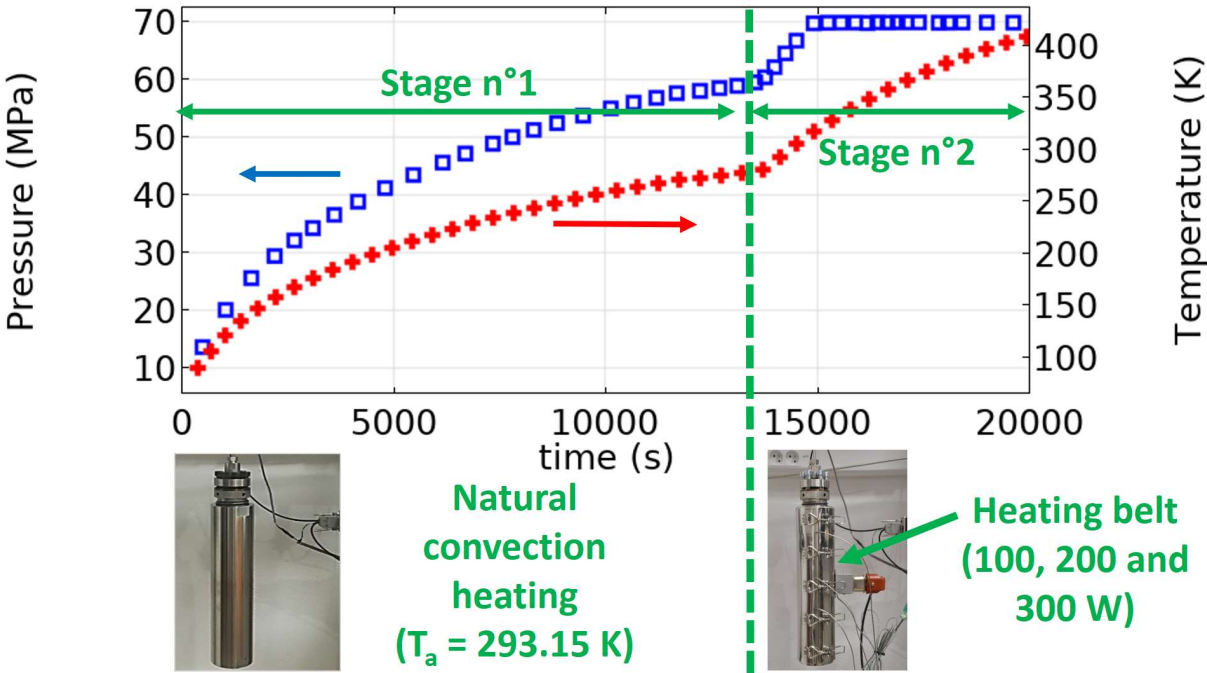


Figure 1: Example of temperature and pressure changes as a function of time, for the two compression stages.

Figure 1 thus shows the experimental configuration of the adsorption-desorption compressor used. The compression tank was a stainless steel (A286) cylinder with an internal volume of

0.5 L. The temperature of the system was measured by a thermocouple placed inside the tank. The internal volume of the cylinder was completely filled with 0.135 kg of AC and compacted by vibration using a Retsch AS 200 analytical shaker (amplitude of 0.5 mm, 3 cycles of 10 min each). The AC was then outgassed at 523 K for 1.5 h using a vacuum pump and a heating belt, and the pressure reached values of about  $10^{-9}$  MPa. Hydrogen was then introduced into the system by connecting a hydrogen cylinder (20 MPa) to the compressor. A BROOKS SLA5850S flowmeter was used to measure the inlet hydrogen, which was up to  $1.5 \text{ NL min}^{-1}$  with an accuracy of  $\pm 1.0\%$  of full scale. During the charging step, the compression tank was placed in a cryogenic storage Dewar filled with 14 L of liquid nitrogen to be uniformly cooled to 77 K. A backpressure regulator was placed downstream of the compression tank to produce a high-pressure hydrogen flow once the desired pressure (70 MPa) was reached. A second BROOKS SLA5850S flowmeter was used to measure the high-pressure hydrogen flow. The whole system was equipped with a discharge valve, a safety valve and a rupture disk to prevent overpressure. A schematic of the experimental setup is given elsewhere [6].

## 2.2. Materials

The activated carbon MAXSORB<sup>®</sup> MSC-30 from Kansai Coke & Chemicals<sup>™</sup> (Japan) was chosen because it has a very high BET specific area ( $A_{BET}$ ) of about  $3300 \text{ m}^2 \text{ g}^{-1}$ . The textural characterization of this material was carried out and presented in our previous study [15], and its main features are shown in Table 1. High  $A_{BET}$  and high pore volumes are both essential to improve the performance of an adsorption-desorption compressor. The tapped density of the selected AC,  $\rho_b$ , was measured by using an AUTOTAP device from Quantachrome Instruments, in accordance with the standard ASTM D8176-18 test method. High-purity (99.999%) hydrogen was used for the compression experiments.

Table 1 – Properties of the MSC-30 activated carbon

Property / units	Symbol	Value	Reference
BET area / $\text{m}^2 \text{g}^{-1}$	$A_{BET}$	3305	[15]
Pore volume / $\text{cm}^3 \text{g}^{-1}$	$V_{TOT}$	1.60	[15]
Skeletal density / $\text{kg m}^{-3}$	$\rho_s$	2200	[7]
Specific heat / $\text{J kg}^{-1} \text{K}^{-1}$	$c_{p,s}$	825	[16]
Thermal conductivity / $\text{W m}^{-1} \text{K}^{-1}$	$\lambda_s$	0.7	[17]
Tapped density / $\text{kg m}^{-3}$	$\rho_b$	270	this study

### 3. Theory and calculation

#### 3.1. Geometry and mesh

Figure 2 shows the two-dimensional axisymmetric geometry used in this study. The inner and outer radii of the compression tank are 0.025 and 0.04 m, respectively, and the thickness of the heating belt is 4.2 mm. The height of the inner tank is equal to 0.256 m, whereas the total height including the tank walls is 0.296 m. At the top, the discharge section has a diameter of 4 mm. The experimental temperature and pressure at the point named TTC and located at (0, 0.239 m), as well as with the hydrogen discharge flow, were recorded.

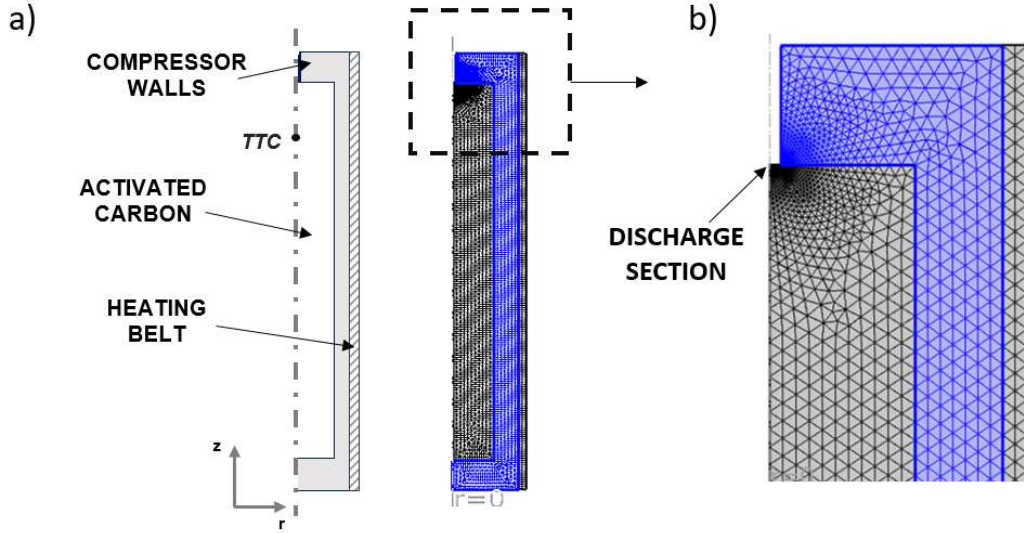


Figure 2: (a) System geometry and finite element mesh used in this work; (b) zoom on the discharge section.

### 3.2. Heat and mass transfer in the activated carbon (AC)

#### 3.2.1. Mass conservation equation

In order to describe the mass balance in our thermally driven compressor, we took into account the contribution of hydrogen in both bulk and adsorbed phases. The following assumptions were made:

- i. The mass source term,  $K_g$ , indicates the amount of hydrogen undergoing a phase change, from the adsorbed phase to the bulk phase.
- ii. The average velocity related to the hydrogen flow through the porous medium,  $\overline{v}_g$ , is described by Darcy's law.
- iii. No volume changes with time,  $t$ .

According to the definitions above, the mass conservation equation for the hydrogen in the bulk phase can be written as:

$$\frac{\partial(\varepsilon_g \rho_g)}{\partial t} + \vec{\nabla} \cdot (\varepsilon_g \rho_g \vec{v}_g) = K_g \quad \text{Eq. 1}$$

where  $\rho_g$  [kg m<sup>-3</sup>] is the bulk density of hydrogen,  $\varepsilon_g$  [dimensionless] is the volume fraction of the hydrogen bulk phase,  $\vec{v}_g$  [ms<sup>-1</sup>] is the average velocity related to the hydrogen flow through the porous medium and  $K_g$  [kg m<sup>-3</sup> s<sup>-1</sup>] is the mass source term as defined above. In the same way, the following mass conservation equation can be written for hydrogen in the adsorbed phase:

$$\frac{\partial(\varepsilon_a \rho_a)}{\partial t} = -K_g \quad \text{Eq. 2}$$

where  $\rho_a$  [kg m<sup>-3</sup>] is the density of adsorbed hydrogen and  $\varepsilon_a$  [dimensionless] is its corresponding volume fraction.

The mass balance related to hydrogen in the adsorbed phase can be written in terms of the absolute amount of hydrogen adsorbed to the total mass of AC,  $m_s$ , contained in the compression tank,  $x_a$  [mol kg<sup>-1</sup>]. Thus, we can write:

$$\varepsilon_a \rho_a = \frac{V_a}{V_{tank}} \frac{x_a m_s M}{V_a} = x_a \rho_b M \quad \text{Eq. 3}$$

where  $V_{tank}$  is the inner volume of the tank,  $\rho_b = \varepsilon_s \rho_s$  [kg m<sup>-3</sup>] is the apparent density of the AC bed ( $m_s / V_{tank}$ ),  $\varepsilon_s [V_s / V_{tank}]$  is the volume fraction occupied by the AC of skeletal volume  $V_s$  (*i.e.*, the volume of solid carbon without taking its pore volume into account), and  $\rho_s$  [kg m<sup>-3</sup>] is the intrinsic, or skeletal, density of the AC ( $m_s / V_s$ ). Finally,  $M$  [kg mol<sup>-1</sup>] is the molecular mass of hydrogen (0.002 kg mol<sup>-1</sup>).

According to the aforementioned assumptions, adding Eq. (1) and Eq. (2) and considering Eq. (3), the overall mass conservation equation reads as follows:

$$\frac{\varepsilon_g \partial \rho_g}{\partial t} + \vec{\nabla} \cdot \left( -\varepsilon_g \rho_g \frac{k}{\mu} \vec{\nabla} P \right) = -\rho_b M \left( 1 - \frac{\rho_g}{\rho_a} \right) \frac{\partial x_a}{\partial t} \quad \text{Eq. 4}$$

where  $k$  [ $\text{m}^2$ ] is the (macroscopic) permeability of the AC (i.e., of the packing of AC grains) and  $\mu$  [ $\text{Pa s}$ ] is the dynamic viscosity of hydrogen.

### 3.2.2. Energy conservation equation

The energy balance expresses the balance between the amount of energy accumulated in the tank and the energy fluctuations mainly due to the conductive heat flux, the heat released during adsorption and the heat exchanged with the external environment. It can be expressed as follows [18]:

$$\frac{\partial(\rho\hat{H})}{\partial t} + (\vec{\nabla} \cdot (\rho\hat{H}\vec{v})) + (\vec{\nabla} \cdot \vec{q}) = Q \quad \text{Eq. 5}$$

where  $\hat{H}$  [ $\text{J kg}^{-1}$ ] is the total enthalpy of the system,  $q$  [ $\text{W m}^{-2}$ ] is the heat flux due to conduction, and  $Q$  [ $\text{W m}^{-3}$ ] is the energy source term. Eq. (5) was applied to two different zones: (i) the active volume of the tank,  $V_{\text{tank}}$ , where hydrogen adsorption and desorption occur, and (ii) the walls of the tank.

Considering the contributions of hydrogen in the bulk and adsorbed phases, as well as the contribution of the AC in the amount of energy accumulated inside the tank, Eq. (5) can be rewritten as follows:

$$\begin{aligned} & (\varepsilon_g c_{p,g} \rho_g + \varepsilon_a c_{p,a} \rho_a + \varepsilon_s c_{p,s} \rho_s) \frac{\partial T}{\partial t} + \vec{\nabla} \cdot \left( -\varepsilon_g \rho_g c_{p,g} T \frac{k}{\mu} \vec{\nabla} P \right) + \\ & \vec{\nabla} \cdot \left( -\lambda_{eff} \vec{\nabla} T \right) = -\varepsilon_g c_{p,g} T \frac{\partial \rho_g}{\partial t} - c_{p,g} \rho_g T \frac{\partial \varepsilon_g}{\partial t} - c_{p,a} \rho_a T \frac{\partial \varepsilon_a}{\partial t} - \rho_b \Delta H_{ads} \frac{\partial \chi_a}{\partial t} \end{aligned} \quad \text{Eq. 6}$$

where  $c_{p,g}$ ,  $c_{p,a}$  and  $c_{p,s}$  [ $\text{J kg}^{-1} \text{K}^{-1}$ ] are the specific heat capacities at constant pressure for hydrogen in the bulk phase, hydrogen in the adsorbed phase, and AC ( $c_{p,s} = 825 \text{ J kg}^{-1} \text{K}^{-1}$ ), respectively.  $\lambda_{eff}$  [ $\text{W m}^{-1} \text{K}^{-1}$ ] is the effective thermal conductivity of the system, and  $\Delta H_{ads}$  [ $\text{J mol}^{-1}$ ] is the heat of adsorption, which is considered constant in the present numerical model.

Since the specific heat ( $c_{p,g}$ ) of hydrogen in the bulk phase depends on pressure and temperature, explicit expressions for  $c_{p,g}$  as a function of pressure and temperature are required to implement variations in the numerical model. Such explicit expressions are rarely presented in the research literature and therefore, data from the NIST Standard Reference Database 23 (software: REFPROP-8®) were fitted using several expressions, depending on the pressure and temperature ranges [19]. Two general expressions for  $c_{p,g}$ , depending on pressure  $P$  [MPa] and temperature  $T$  [K] were obtained for two distinct temperatures ranges: [77-175K] and [175-450 K].

Considering the [77-175K] temperature range, the expression is the following one (Eq. 7):

$$\begin{aligned}
 c_{p,g}(T, P) &= 1000 [a(T)P^5 + b(T)P^4 + c(T)P^3 + d(T)P^2 + e(T)P + f(T)] \\
 a(T) &= 14522.96 T^{-5.91} \\
 b(T) &= -245297.13 T^{-5.33} \\
 c(T) &= 952790.1 T^{-4.64} \\
 d(T) &= -828788.6 T^{-3.78} \\
 e(T) &= 90788.22 T^{-2.66} \\
 f(T) &= 0.0277 T + 8.33
 \end{aligned}
 \tag{Eq. 7}$$

where  $a(T)$ ,  $b(T)$ ,  $c(T)$ ,  $d(T)$ ,  $e(T)$  and  $f(T)$  are the temperature-dependent coefficients.

Considering the [175-450K] temperature range, the expression as follows (Eq. 8):

$$\begin{aligned}
 c_{p,g}(T, P) &= 1000(A(T)\exp\left(\frac{P}{B(T)}\right) + y_0(T)) \\
 A(T) &= -3.93 e^{\left(\frac{T}{-146.38}\right)} + 0.269 \\
 B(T) &= 103.5 e^{\left(\frac{T}{-525.7}\right)} - 86.7 \\
 y_0(T) &= -1.97 \cdot 10^{-1} T^4 + 3.36 \cdot 10^{-7} T^3 - 2.14668160183 \cdot 10^{-4} T^2 \\
 &\quad + 5.95 \cdot 10^{-2} T + 9.07
 \end{aligned}
 \tag{Eq. 8}$$

where  $A(T)$ ,  $B(T)$  and  $y_0(T)$  are temperature-dependent coefficients. The regression curves are given in the Supporting Information (Figures SI 1.a) and SI 1.b)). The quality of the regression was confirmed both by observing the determination coefficient  $R^2$  for each step (pressure and temperature) of the regression and by checking the residuals. The latter were strictly less than 1.5 % (Figures SI 1.c) and SI 1.d)) while the values of  $R^2$  were all above the usual acceptance limit of 0.99.

On the other hand, the temperature dependence of  $c_{p,a}$  [ $\text{J kg}^{-1} \text{K}^{-1}$ ] was evaluated in our previous study [15]:

$$c_{p,a} = -5.3 \cdot 10^{-2} T^2 + 33.5 \cdot T + 3698.1 \quad \text{Eq. 9}$$

$\lambda_{eff}$  was calculated by considering the contribution of each component to the overall heat transfer. Two expressions were considered: (i) a parallel model; and (ii) a series model. In this way, the upper and lower limit of the thermal conductivity of a porous medium were calculated, respectively.

- Parallel model:

$$\lambda_{eff} = \varepsilon_g \lambda_g + \varepsilon_a \lambda_a + \varepsilon_s \lambda_s \quad \text{Eq. 10}$$

- Series model:

$$\lambda_{eff} = \frac{1}{\varepsilon_g / \lambda_g + \varepsilon_a / \lambda_a + \varepsilon_s / \lambda_s} \quad \text{Eq. 11}$$

where  $\lambda_g$ ,  $\lambda_a$  and  $\lambda_s$  [ $\text{W m}^{-1} \text{K}^{-1}$ ] are the thermal conductivities of the bulk hydrogen phase, adsorbed hydrogen phase, and AC, respectively. The temperature dependence of  $\lambda_g$  was calculated from NIST data and for a pressure near 3 MPa (close to the maximum excess uptake on MSC-30 at 77 K) using the software REFPROP-8®:

$$\lambda_g = 5.40 \cdot 10^{-4} T + 0.02426 \quad \text{Eq. 12}$$

This simple expression was compared to a polynomial model dependent on pressure and temperature (SI Note 1 and Figure SI 1.a)). The quality of the regression, based on NIST values, and the use of the polynomial model met the usual acceptance limit  $R^2 > 0.99$  (SI score 1, Figures SI 1.a) and SI 1.b)). Furthermore, the difference between the thermal conductivity values obtained from the polynomial expression and the NIST values was found to be less than 5% (Figure SI 1.c)) in the ranges 1 - 70 MPa and 77 - 400 K. Finally, the difference between the values obtained using Eq. (12) and the above polynomial model was found to be very small (*i.e.*,  $< 0.073 \text{ W m}^{-1} \text{ K}^{-1}$ ) when compared, as a function of temperature, to the other thermal conductivities (Figure SI 1.d)). Consequently, the effect of using Eq. (12), instead of the polynomial model, on the overall thermal conductivity was assumed to lead to minor errors. For this the reason, Eq. (12) was used here instead of the polynomial model.

$\lambda_a$  was considered equal to the thermal conductivity of hydrogen in the liquid phase and its temperature dependence was found in the literature [20]:

$$\lambda_a = (7.12 + 0.233T) \cdot 10^{-2} \quad \text{Eq. 13}$$

On the other hand,  $\lambda_s$  was considered as constant in the present work ( $0.7 \text{ W m}^{-1} \text{ K}^{-1}$ ) [17].

### 3.2.3. *Hydrogen equation of state and adsorption equation*

In order to account for the deviation from the ideal conditions due to the high pressures reached during compression, the Van der Waals equation was chosen out of all other possible equations of state for hydrogen [21]:

$$\left( P + \frac{an_g^2}{V_g^2} \right) (V_g - n_g b) = n_g RT \quad \text{Eq. 14}$$

where  $a$  and  $b$  are the constant parameters of the Van der Waals equation ( $0.02476 \text{ J m}^3 \text{ mol}^{-2}$  and  $2.661 \times 10^{-5} \text{ m}^3 \text{ mol}^{-1}$ , respectively) and  $R$  is the universal gas constant,  $8.314 \text{ J m}^3 \text{ Pa K}^{-1}$

mol<sup>-1</sup>). To increase the computational speed using the Comsol™ software for the simulations, the derived form of Eq. (14) was used:

$$\frac{\partial P}{\partial t} = \frac{R}{\left(\frac{M}{\rho_g - b}\right)} \frac{\partial T}{\partial t} + \left( \frac{RTM}{(M - \rho_g b)^2} - \frac{2a\rho_g}{M^2} \right) \frac{\partial \rho_g}{\partial t} \quad \text{Eq. 15}$$

The modified Dubinin-Astakhov (MDA) equation proposed by Richard et al. [22] proved to be a good analytical tool for representing experimental data on the adsorption of different gases over a wide range of pressures and temperatures under supercritical conditions, particularly in the case of hydrogen adsorption on ACs [7,23]:

$$x_a = x_{max} \exp \left( - \left( \frac{RT}{\alpha + \beta T} \right)^2 \ln^2 \left( \frac{P_s}{P} \right) \right) \quad \text{Eq. 16}$$

Eq. (16) gives the evolution of the absolute amount of hydrogen adsorbed as a function of pressure and temperature, with higher amounts of hydrogen being adsorbed at higher pressures and lower temperatures [24]. The model requires 5 parameters:  $x_{max}$  [mol kg<sup>-1</sup>] is the amount of adsorbed hydrogen corresponding to the saturation of the entire available pore volume,  $\alpha$  [J mol<sup>-1</sup>] is an enthalpy factor,  $\beta$  [mol J<sup>-1</sup> K<sup>-1</sup>] is an entropy factor [25], and  $P_s$  [MPa] is the pseudo-saturation pressure [15,26,27].

### 3.2.4. Initial and boundary conditions

The hydrogen discharge flow,  $\dot{n}_{out}$  [kg m<sup>-2</sup> s<sup>-1</sup>], obtained once the desired 70 MPa was reached, was simulated using the following expression:

$$\dot{n}_{out} = h_m (P_{max} - P) \quad \text{Eq. 17}$$

where  $P_{max}$  [MPa] is the fixed maximum pressure (70 MPa),  $P$  [MPa] is the hydrogen pressure inside the tank, and  $h_m$  [kg m<sup>-2</sup> s<sup>-1</sup> Pa<sup>-1</sup>] is a constant relating the discharge flow to the pressure difference, and considered as a fitting parameter.

In addition, heat is also released from the system by  $\dot{n}_{out}$  and this contribution was calculated as follows:

$$\dot{Q}_{flow} = \dot{n}_{out} c_{p,g} T \quad \text{Eq. 18}$$

Finally, the tank is subject to convective heat flux with the surrounding environment,  $\dot{Q}$  [W m<sup>-2</sup>], which is determined by the following expression:

$$\dot{Q} = h_c (T_F - T) \quad \text{Eq. 19}$$

where  $h_c$  [W m<sup>-2</sup> K<sup>-1</sup>] is the global heat transfer coefficient, and  $T_F$  [K] is the temperature of the surrounding environment (293 K).

### 3.3. Heat transfer in the tank walls and in the heating belt

The heat transfer equation was then applied to the tank walls with conductive heat flux:

$$\rho_w c_{p,w} \frac{\partial T}{\partial t} + \vec{\nabla} \cdot (-\lambda_w \vec{\nabla} T) = Q \quad \text{Eq. 20}$$

where  $\rho_w$  [kg m<sup>-3</sup>] is the density,  $c_{p,w}$  [J kg<sup>-1</sup> K<sup>-1</sup>] is the specific heat capacity, and  $\lambda_w$  [W m<sup>-1</sup> K<sup>-1</sup>] is the thermal conductivity of the wall and the heating belt, assumed here to be identical for simplicity, as both are metallic structures. We also assumed that the thermal properties of the A286 stainless steel used were equivalent to those of the AISI 304 stainless steel. Hence, the thermal dependence of  $c_{p,w}$  was found in the literature [28] and can be fitted by the following equation:

$$c_{p,w} = 143.68 \log(T) - 370.51 \quad \text{Eq. 21}$$

$\rho_w$  and  $\lambda_w$  were considered constant with respect to temperature.  $Q$  is the power density [W m<sup>-3</sup>] applied to the heating belt and considered as the ratio of the electrical power applied to the heating resistors (100, 200 or 300 W) to the volume of the belt ( $Q$  takes a zero value in the tank walls).

### 3.4. Implementation of the numerical method

The entire system of equations presented in this section was solved using Comsol<sup>TM</sup> software. The three dependent variables were thus  $\rho_g$ ,  $P$  and  $T$  and the parameters used for the present numerical simulation are listed in Table 2.

An extremely fine mesh consisting of 5332 triangles and 2806 vertices was used. The mesh was refined at the discharge section to improve the prediction of the high-pressure hydrogen flow out of the compression tank (Figure 2b). Each simulation required a computational time of 92 seconds and the simulations were run for 450 minutes of the compression process.

Table 2 – Constant parameters used in the present numerical model

Parameter / units	Symbol	Value	Reference
A286 density / kg m <sup>-3</sup>	$\rho_w$	7950	[29]
A286 specific heat / J kg <sup>-1</sup> K <sup>-1</sup>	$c_{p,w}$	460	[29]
A286 thermal conductivity / W m <sup>-1</sup> K <sup>-1</sup>	$\lambda_w$	12	[29]
Enthalpy factor in MDA equation / J mol <sup>-1</sup>	$\alpha$	3300	[15]
Entropy factor in MDA equation / J mol <sup>-1</sup> K <sup>-1</sup>	$\beta$	15.79	[15]
Global heat transfer coefficient / W m <sup>-2</sup> K <sup>-1</sup>	$h_T$	40	this study
Heat of adsorption / J mol <sup>-1</sup>	$\Delta H_{ads}$	-6,000	[15]
Hydrogen viscosity (293.15 K and 1 atm) / Pa·s	$\mu$	$9 \cdot 10^{-6}$	[30]
Maximum hydrogen adsorbed / mol kg <sup>-1</sup>	$x_m$	72.46	[15]
Permeability / m <sup>2</sup>	$k$	$10^{-11}$	this study
Pseudo-saturation pressure / MPa	$P_s$	1013	[15]
Total volume of tank / m <sup>3</sup>	$V_{tank}$	$5 \cdot 10^{-4}$	this study

## 4. Results and discussion

### 4.1. Parametric study

#### 4.1.1. *Impact of the hydrogen density in the adsorbed phase*

The hydrogen density in the adsorbed phase has not been clearly determined in the literature. If the density of the liquid phase is taken as a reference, its value would be equal to  $71 \text{ kg m}^{-3}$ . Some authors estimated a density for the adsorbed phase higher than that of the liquid phase ( $80 \text{ kg m}^{-3}$  for a temperature of 50 K and a pressure of 7 MPa) [31], while other works suggested that the density of hydrogen adsorbed in AC is a function of the pore size with an upper limit equal to the density of the liquid phase [32]. In order to understand the impact of the density of the adsorbed hydrogen on the performance of the adsorption/desorption compressor, a parametric study was performed. Thus, the density of adsorbed hydrogen was varied from 50 to  $90 \text{ kg m}^{-3}$ . Figure 3a shows that the simulation is not affected by the density value of the adsorbed phase. Indeed, the final pressure varies from 52.3 to 53.1 MPa before the electrical resistor heating. A total variation of 1.5% compared to the absolute value of 52.9 MPa was obtained by considering an adsorbed density equal to  $70 \text{ kg m}^{-3}$ . Finally, the time evolution of the pressure inside the tank was identical for all cases (Figure 3b), while the time evolution of the temperature was only slightly affected by the value of the density of the adsorbed phase (Figure 3c). Therefore, the value of the liquid hydrogen density ( $71 \text{ kg m}^{-3}$ ) was selected for the rest of the simulations presented in this study.

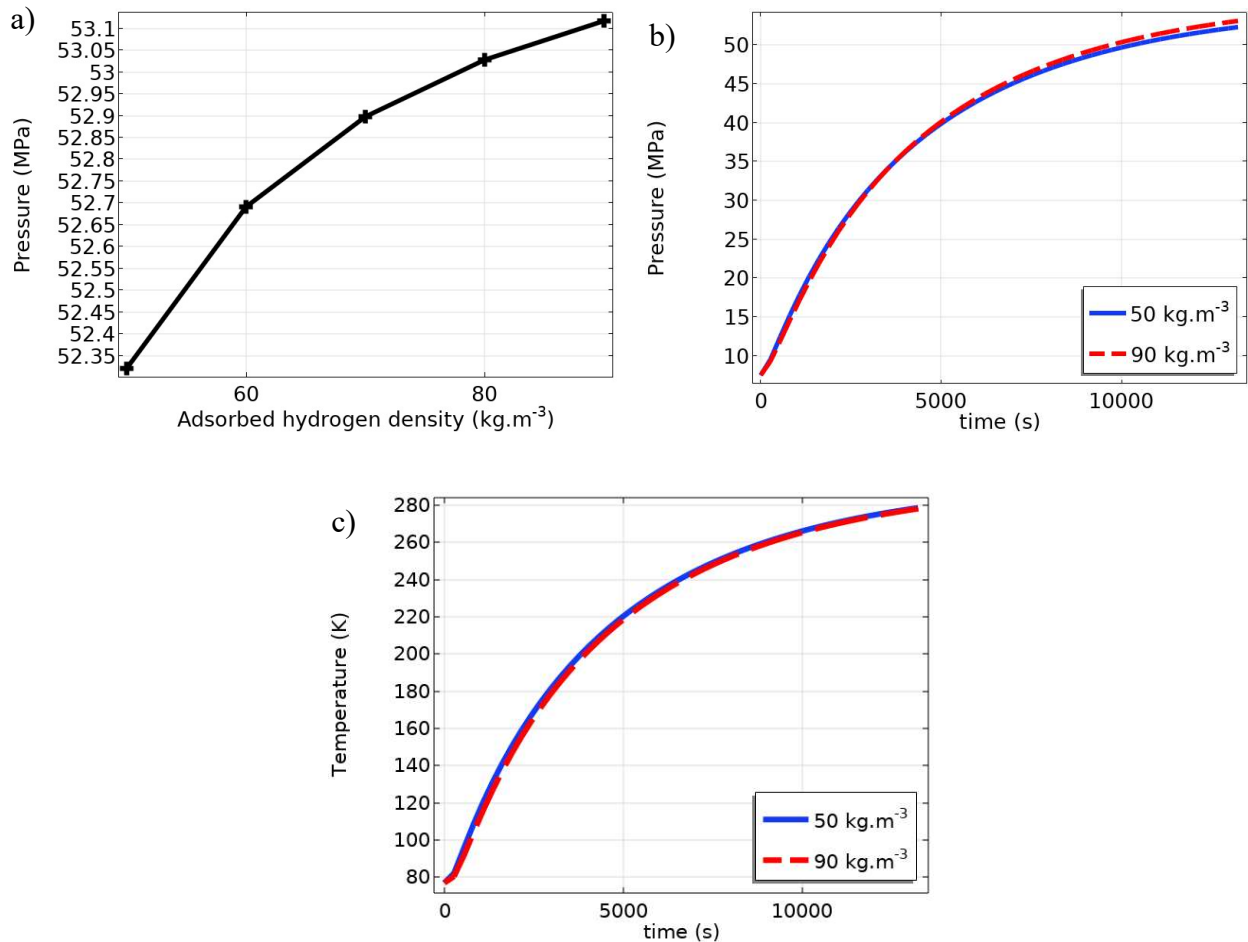


Figure 3: (a) Pressure at the end of the first stage as a function of the density of adsorbed hydrogen; Time evolution of: (b) pressure; and (c) temperature inside the tank.

#### 4.1.2. Impact of the mass transfer coefficient

The second parametric study concerns the mass transfer coefficient,  $h_m$ , which can be compared to a pressure drop coefficient of the discharge valve, and which can only be obtained by fitting the experimental data. It can be observed that the lower this coefficient, the lower the discharge flow (Figure 4a) and, conversely, the higher the pressure inside the compressor even after the valve is opened (Figure 4b). Indeed, for low discharge flow (Figure 4a), the hydrogen pressure continues to increase according to Van der Waals law (Figure 4b). When the temperature reaches equilibrium, still with a low discharge flow ( $h_m = 3 \cdot 10^{-9} \text{ kg m}^{-2} \text{ s}^{-1} \text{ Pa}^{-1}$ ), the mass loss overcomes the temperature increase, resulting in a pressure drop in the compressor

(Figure 4b). It should be noted that as  $h_m$  tends to infinity, which is equivalent to imposing the pressure at boundary conditions.

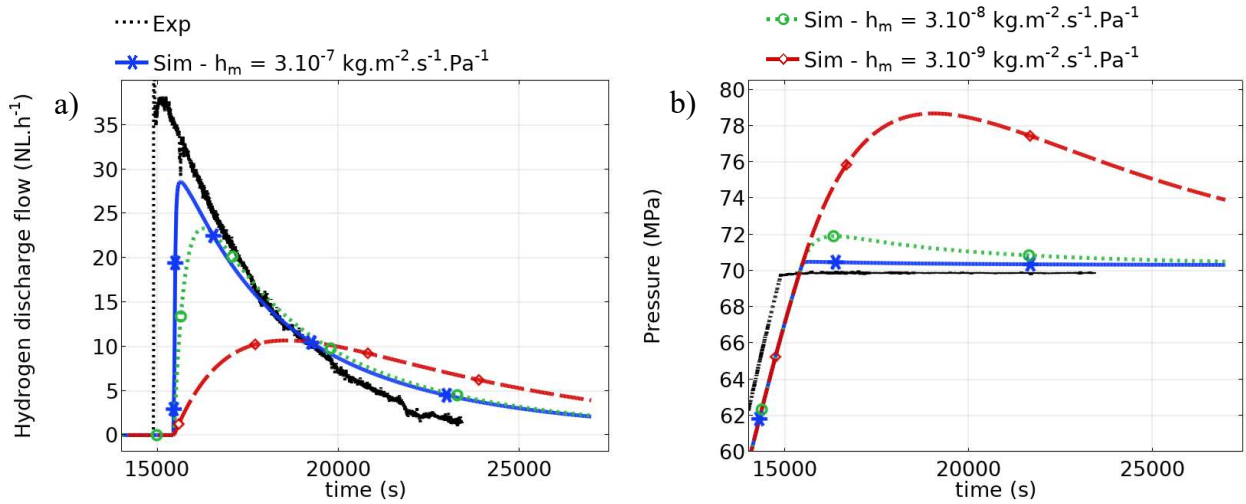


Figure 4. (a) Predicted hydrogen discharge flow; and (b) pressure, as a function of time for different values of  $h_m$ , and compared to the experimental data.

#### 4.1.3. Impact of the thermal conductivity

Both a parallel and a series model were used to understand the impact of the multiphase thermal conductivity model on the simulation results, as described in Section 3. The results on temperature (Figure 5a), pressure (Figure 5b), and hydrogen discharge flow (Figure 5c) show negligible impact of thermal conductivity models on these kinetics. These two models allow the calculation of the maximum and minimum value of the thermal conductivity of a porous medium. It can be observed that a maximum factor of two exists between these two models (Figure 5d), which is not enough to impact the results. A variation of a factor of 10 would be required to observe an impact. By default, a parallel model is used, and it will be used for the rest of the simulations. Furthermore, the model is not very sensitive to the thermal conductivity of the AC because the exchange with the outside is very low and therefore limiting. This will not be the case in an industrial compressor where the exchange with the outside will be much

more efficient. It will then be limited by the thermal conductivity of the AC as in the case of hydride compressors [33].

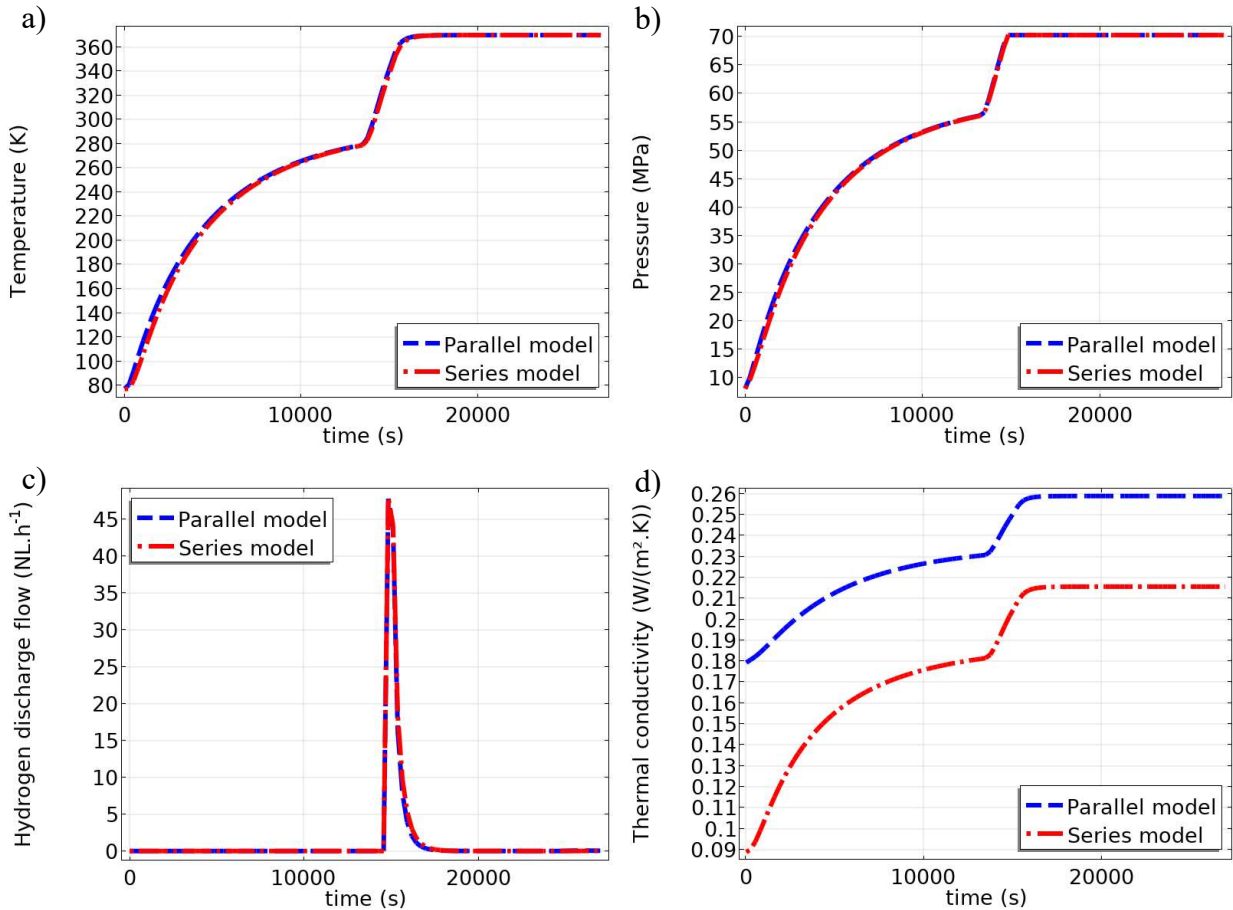


Figure 5 : (a) Predicted temperature; (b) pressure; (c) hydrogen discharge flow; and (d) thermal conductivity, assuming either a parallel or a series model.

## 4.2. Validation of the model

### 4.2.1. Time evolutions of temperature, pressure and discharge flow

The model was validated by comparison with the experimental evolution of temperature (Figure 6a, b, c), pressure (Figure 6d, e, f), flow of hydrogen delivered by the compressor (Figure 6g, h, i), quantity of hydrogen delivered (Figure 6j, k, l) and temperature at the surface of the heating belt (Figure 6m, n, o), for three applied powers, namely 100, 200 and 300 W.

The observed trends are the same according to the powers applied to the heating belt. During step 1, the increase in the tank temperature is driven by natural convection (Figure 6a, b, c). The differences between the experimental and simulated temperatures are small, although a slight overestimation can be observed with the simulation. Hydrogen desorption triggered by the increase in tank temperature leads to an exponential increase in hydrogen pressure inside the tank (Figure 6d, e, f). The differences between the measured and simulated pressures are also small; a slight overestimation of the pressure can be observed during the temperature rise, as well as an underestimation at the end of the temperature rise (minus 5 MPa compared to the experimental value).

During step 2, the heating belt is installed when the temperature in the tank is between 273 and 278 K. The equilibrium with the outside temperature (293 K) is deliberately not reached for time-saving reasons. Once the belt is in place, the temperature in the tank (Figure 6a, b, c) and at the surface (Figure 6m, n, o) increases with a model response very close to the experimental evolution. For a power of 100 W, the temperature tends towards 373 K while for 200 and 300 W it exceeds 423 K. The above values are not shown because the temperature sensor in the tank is limited to 423 K for safety reasons. As in step 1, the pressure continues to increase with temperature until it reaches 70 MPa, at which point the compressor opens (Figure 6d, e, f). For all powers, a time lag is observed when the discharge valve opens compared to the experimental values (Figure 6g, h, i). This time lag is explained by the underestimation of the predicted pressure observed at the end of step 1. Despite this offset, the predicted discharge flow is very close to the experimental one, with a high flow at the opening of the discharge valve, and a decreasing trend over time (Figure 6g, h, i).

For steps 1 and 2, the model shows a response very close to the experimental evolutions for the three cases studied, which makes it possible to validate the hypotheses chosen and the implementation carried out (software, meshing, etc.).

In step 1, the power has no impact since the heating belt is not applied. After installation, three heating powers were tested: 100, 200 and 300 W. It can be observed that the higher the power, the higher the amount of hydrogen delivered by the compressor (0.4, 1.6 and 2.2 mol at the end of the simulation for 100, 200 and 300 W respectively) and the earlier the discharge takes place (20 000, 15 500 and 14 800 s for 100, 200 and 300 W, respectively) (Figure 6j, k, l). The increase in power raises the temperature of the compressor and accelerates the heat transfer. At constant power, the temperature inside the compressor increases continuously. As the temperature increases more at higher power, the hydrogen seeks to expand with the only escape being the discharge to the outside at 70 MPa, which explains the greater amount of hydrogen discharged. In addition, as the temperature increases more rapidly with power, the pressure reaches the 70 MPa value earlier and the discharge valve therefore opens earlier.

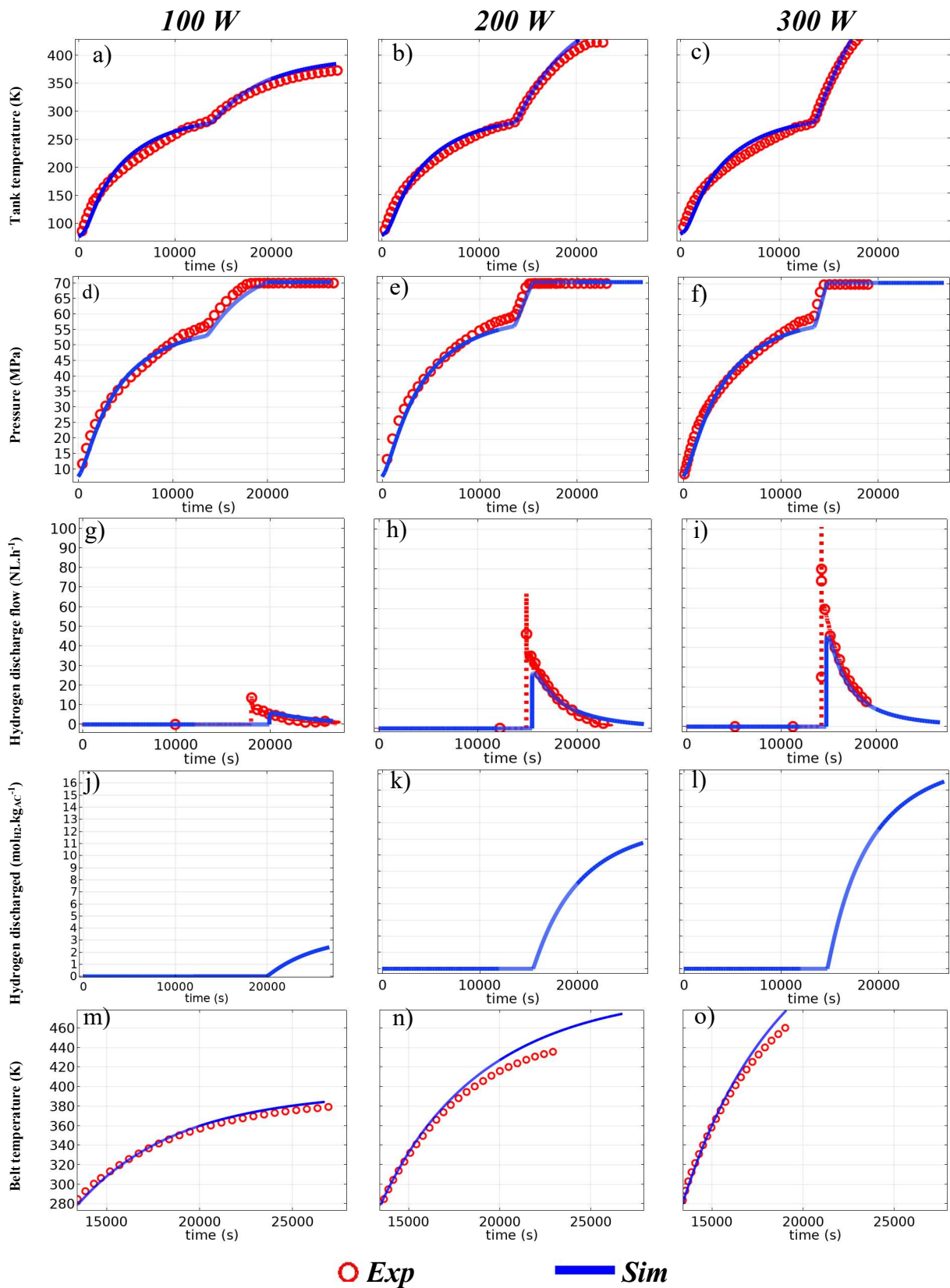


Figure 6. Predicted (solid line) and experimental (empty circles) evolution of the temperature (a, b, c), pressure (d, e, f), hydrogen flow supplied by the compressor (g, h, i), amount of hydrogen discharged (j, k, l) and temperature at the surface of the heating

belt (m, n, o), for the three applied powers: 100 W - first column, 200 W - second column, and 300 W - third column.

#### **4.2.2. Analysis of the opening of the discharge valve**

The opening of the discharge valve when the pressure reaches 70 MPa is a sudden phenomenon, characterized by a hydrogen flow passing from zero to the maximum flow (50 NL h<sup>-1</sup> with a power of 300 W) in a few seconds (Figure 6g, h, i). The simulations show a cooling phenomenon at the compressor outlet when the discharge valve is opened (Figure 7a). This phenomenon loses its magnitude with depth, where no cooling is observed but only a variation of the predicted temperature evolution with time (Figure 7b). No thermocouple is placed at the compressor outlet, which makes it impossible to measure this phenomenon.

Nevertheless, a thermocouple is placed at 17 mm from the outlet and also allows to observe a very marked decrease of the temperature variation ( $dT/dt$ ) when the discharge valve is opened (Figure 7c, d), which is also observed with the simulation. Moreover, this phenomenon becomes more and more important by increasing the applied power, since it is not observable at 100 W, visible at 200 W (Figure 7c) and accentuated at 300 W (Figure 7d). By plotting on a 2D surface the derivative of temperature versus time at moments close to the opening of the discharge valve (Figure 7e represents the moment just before the opening, Figure 7f the first moment recorded after the opening, and Figure 7g the second moment recorded after the opening), one can observe that this phenomenon is very localized, close to the compressor outlet, and that the hydrogen flow (black arrows) is very important at this point. One could imagine that this phenomenon is explained by the energy linked to the desorption of hydrogen during the opening of the tank, but the simulation shows that the amount of adsorbed hydrogen increases at the interface at this moment.

A study was carried out without taking into account the heat of adsorption and a low impact was observed on the temperature (Figure SI ), which always decreased and concluded that this

phenomenon was not related to the hydrogen desorption upon opening. The second hypothesis to explain this phenomenon concerns the impact of gas transfer from the inside to the outside. Indeed, when the compressor opens, the temperature is not uniform, with a lower temperature in the center than on the peripheral parts of the tank (Figure 7a). Upon opening, the colder gas in the center moves towards the warmer outlet area, thus reducing its temperature.

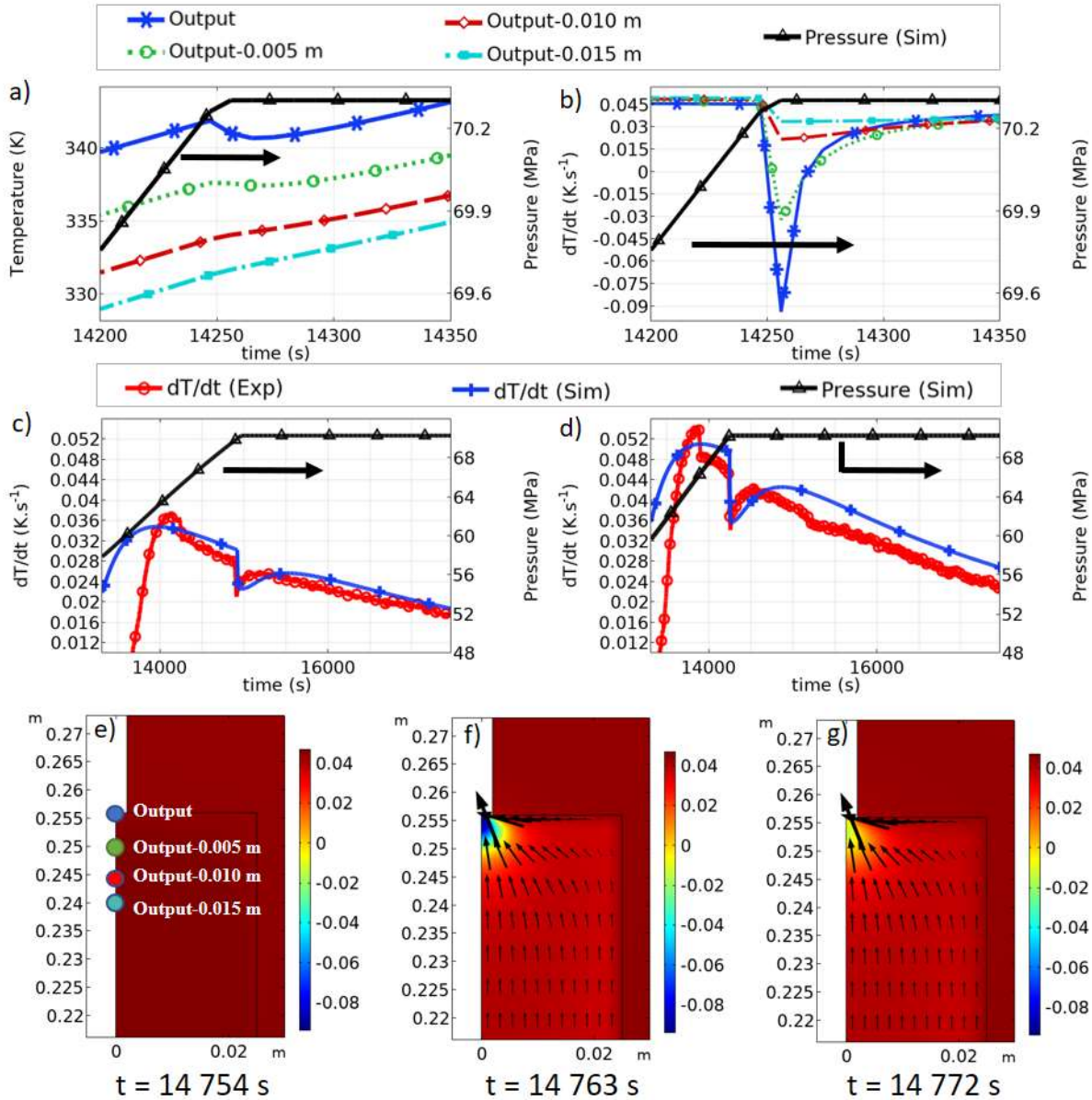


Figure 7. Evolution of: (a) temperature and (b) and temperature derivative,  $dT / dt$ , as a function of time simulated at four points on the axys of symmetry when the compressor is opened; (c) Numerical (blue solid line) and experimental (red circle)

evolution of the temperature derivative ( $dT / dt$ ) at 200 W; and (d) at 300 W. 2D mapping of the simulated temperature derivative -  $dT / dt$  (300W) - at three times: (e) 14 754 s; (f) 14 763 s; and (g) 14 772 s; the arrows represent the hydrogen gas flow.

### **4.3. Influence of external conditions**

In this section, the model is used to simulate the behavior of the compressor when varying external conditions such as final temperature or heat exchange coefficient. These extrapolated results are only valid for this simulation setting. Indeed, a discrepancy between the simulations and the experimental evolutions has been observed in the previous section. Although the model remains robust, the absolute values should be taken with caution, nevertheless the general trends should be representative.

#### ***4.3.1. Effect of the set temperature***

Here, the impact of the set temperature, from 313 to 473 K, on the compressor performance is studied by varying the heating power between 0 and 300 W. The heating step to room temperature is the same for all simulations and thus, no difference was observed for the time evolution of temperature and pressure (Figure 8d and f). As in the previous tests, once the temperature between 273 and 278 K is reached, the heating belt is installed for final heating and to reach the pressure of 70 MPa. Simulations show that for set temperatures of 313 – 333 K, the pressure of 70 MPa is not reached (Figure 8e and f). However, the pressure of 70 MPa is reached for temperatures above 333 K. Above this temperature, the pressure profiles are identical to the one corresponding to the simulation at 343 K, which is why they are not shown (Figure 8f). The compressor outlet flow has the same evolution as for the previous simulations with a high flow as soon as the discharge valve is opened, followed by a decrease (Figure 8a and b). The difference is a faster decrease when the set temperature is reached (Figure 8b). In

fact, as long as the temperature is lower than the set temperature ( $T < T_{set}$ ), the power supplied by the control is maximum (300 W), the system is in the same case as at constant power and the output flow shows the same profile (Figure 6i). When the temperature reaches the set temperature, the power supplied to the compressor decreases, which leads to a reduction in the output flow (Figure 8b). Thus, the longer the power remains at its maximum value and the higher the temperature, the later the flow decreases, resulting in an increase in the amount of hydrogen released by the compressor (Figure 8c). Through simulation, and in this temperature range, we can observe a quasi-linear relationship between the amount of hydrogen discharged and the set temperature as long as it is below 500K, which confirms that the higher the set temperature, the more hydrogen is released (Figure 8e). At 343 K, the amount of hydrogen discharged is  $0.27 \text{ mol}_{\text{H}_2}/\text{kg}_{\text{AC}}$  (0.54 wt%) and if the temperature were set to 473.15K, this amount would reach  $11 \text{ mol}_{\text{H}_2}/\text{kg}_{\text{AC}}$  (2.2 wt.%). At very high, and impractical temperatures, the amount of hydrogen discharged reaches an asymptote at  $55 \text{ mol}_{\text{H}_2}/\text{kg}_{\text{AC}}$  (11wt. %), see Figure SI 4, in good agreement with the large hydrogen storage capacity of MSC-30 [34].

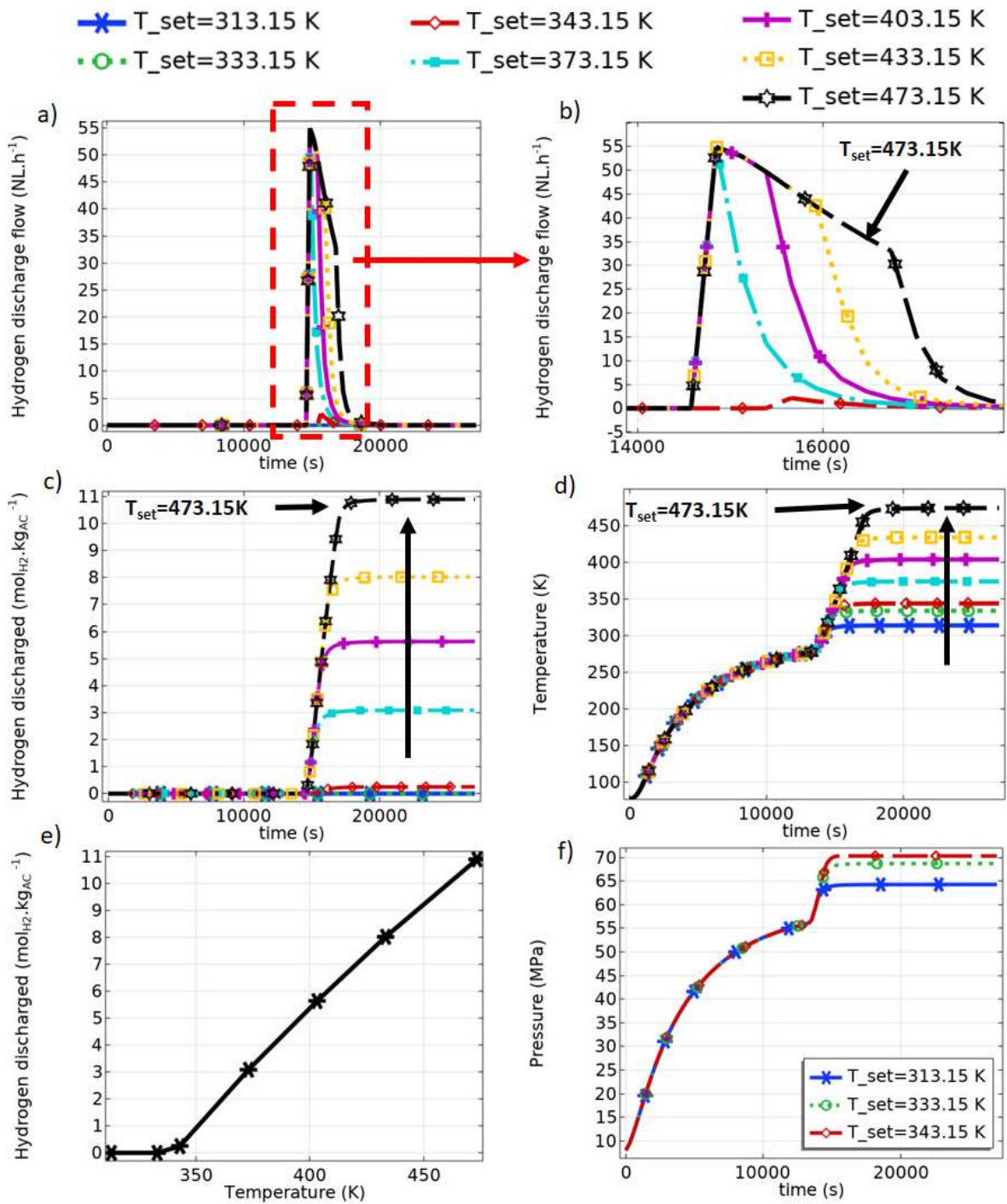


Figure 8. Impact of the set temperature on the time evolution of: (a and b) hydrogen discharge flow; (c) total hydrogen discharged; (d) tank temperature at the location point named TTC; and (f) pressure in the tank. The total amount of hydrogen discharged per kg of AC as a function of the set temperature is plotted in (e).

#### **4.3.2. Effect of intensifying the heat flow by natural convection**

In this simulation, the power provided by the heating belt is suppressed ( $Q = 0$ ) and the heat is supplied by the air through natural convection. The objective is to study the impact of the increased heat flow on the compressor by varying the flow regime of the air surrounding the compressor and thus varying the heat exchange coefficient,  $h_t$ , to 10, 20, 50 and 100 W m<sup>-2</sup> K<sup>-1</sup>. The outside temperature was set to 293 K during step 1 and to 373 K during step 2.

As  $h_t$  increases, the temperature and pressure rise becomes faster for steps 1 and 2 (Figure 9c and d), the outlet flow increases (Figure 9a), and the discharge process takes place over a shorter period of time (Figure 9a) to reach the same amount of hydrogen discharged at the end of the compression step (Figure 9b).

The temperature rise in step 1 is achieved without any heat input other than the heat exchange between the tank and the ambient air. The first tests were carried out in natural convection with a low exchange coefficient ( $h_t = 10$  W m<sup>-2</sup> K<sup>-1</sup>), resulting in a fairly long temperature rise. The simulation shows that by increasing the convection around the tank, a time saving,  $\Delta t$ , of about 10,000s (2.77 h) is observed. This result is extremely relevant because 2.77 h is about 75% of the duration of step 1.

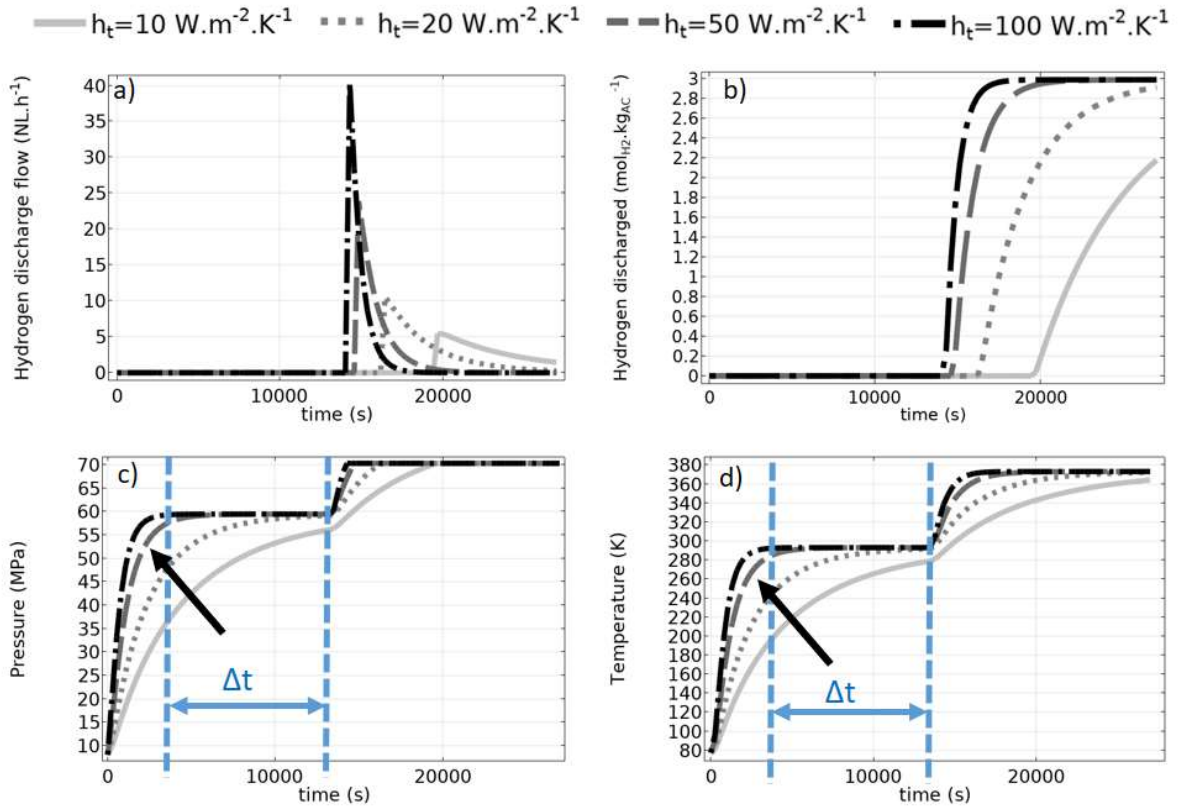


Figure 9. Time evolution of: (a) simulated hydrogen discharged flow; (b) amount of hydrogen discharged; (c) pressure; and (d) temperature, for  $h_t = 10$  (solid), 20 (dotted), 50 (dashed) and 100 (dotted/dashed)  $W \cdot m^{-2} \cdot K^{-1}$ .

## 5. Conclusion

The modeling of a non-mechanical hydrogen compressor based on cyclic adsorption-desorption of hydrogen on activated carbon (AC) was successfully completed. We clearly showed that the value of the density of adsorbed hydrogen had little impact on the results obtained and therefore the value of the density of liquid hydrogen was used for the simulations. The model was able to accurately predict pressure, temperature and discharge flow for three heating powers (100, 200 and 300 W) used to promote hydrogen desorption. A temperature variation was observed experimentally during the compressor discharge and explained by the

simulation. It is due to heat transfer from the colder center to the warmer periphery of the compressor, linked to the mass transfer induced by the discharge.

The predictive character of the model is a step forward for future large-scale sizing of hydrogen compression by thermally driven adsorption-desorption. The parametric study performed on heat transfer provides significant contributions to this new body of knowledge, as follows:

- The more the power, and thus the temperature, is increased, the more hydrogen is discharged.
- The variation in the amount of hydrogen discharged is quasi-linear with respect to the final set temperature, as long as it is below 500K.
- The increase in heat transfer by convection with the outside air would allow to reduce significantly the compression time, by about 75%, which shows the necessity to optimize the heat transfers in the case of an industrial compressor.

After studying the heat transfer outside the compressor, further studies are conducted to investigate the effect of the physicochemical characteristics of the AC, the cyclability of the process and to optimize the heat transfer inside the AC bed by the addition of conductive materials or the use of internal exchangers, among others.

## **Acknowledgment**

This study was supported by the French PIA project “Lorraine Université d’Excellence”, reference ANR-15-IDEX-04-LUE, and the TALiSMAN project, funded by ERDF (2019-000214).

## References

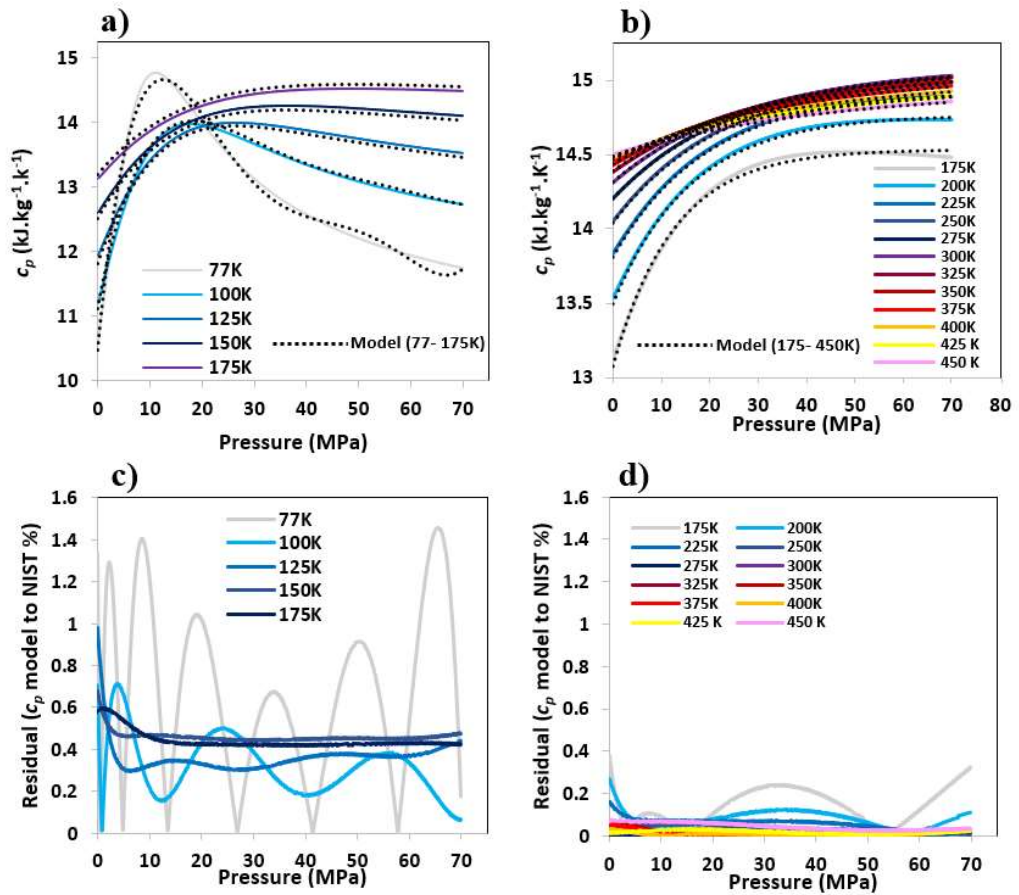
- [1] S. Zhang, L.H. Lee, Y. Sun, Y. Liu, *Materials for Hydrogen Mobile Storage Applications*, IOP Conf. Ser.: Earth Environ. Sci. 632 (2021) 052087. <https://doi.org/10.1088/1755-1315/632/5/052087>.
- [2] B. Sakintuna, F. Lamari-Darkrim, M. Hirscher, *Metal hydride materials for solid hydrogen storage: A review*, *International Journal of Hydrogen Energy*. 32 (2007) 1121–1140. <https://doi.org/10.1016/j.ijhydene.2006.11.022>.
- [3] L. Schlapbach, A. Züttel, *Hydrogen-storage materials for mobile applications*, *Nature*. 414 (2001) 353.
- [4] Q. Hou, X. Yang, J. Zhang, *Review on Hydrogen Storage Performance of MgH<sub>2</sub>: Development and Trends*, *ChemistrySelect*. 6 (2021) 1589–1606. <https://doi.org/10.1002/slct.202004476>.
- [5] G. Sdanghi, G. Maranzana, A. Celzard, V. Fierro, *Review of the current technologies and performances of hydrogen compression for stationary and automotive applications*, *Renewable and Sustainable Energy Reviews*. 102 (2019) 150–170. <https://doi.org/10.1016/j.rser.2018.11.028>.
- [6] G. Sdanghi, V. Nicolas, K. Mozet, S. Schaefer, G. Maranzana, A. Celzard, V. Fierro, *A 70 MPa hydrogen thermally driven compressor based on cyclic adsorption-desorption on activated carbon*, *Carbon*. 161 (2020) 466–478. <https://doi.org/10.1016/j.carbon.2020.01.099>.
- [7] M.-A. Richard, D. Cossement, P.-A. Chandonia, R. Chahine, D. Mori, K. Hirose, *Preliminary evaluation of the performance of an adsorption-based hydrogen storage system*, *AIChE J.* 55 (2009) 2985–2996. <https://doi.org/10.1002/aic.11904>.
- [8] G. Sdanghi, V. Nicolas, K. Mozet, G. Maranzana, A. Celzard, V. Fierro, *Modelling of a hydrogen thermally driven compressor based on cyclic adsorption-desorption on activated carbon*, *International Journal of Hydrogen Energy*. 44 (2019) 16811–16823. <https://doi.org/10.1016/j.ijhydene.2019.04.233>.
- [9] G. Hermosilla-Lara, G. Momen, P.H. Marty, B. Le Neindre, K. Hassouni, *Hydrogen storage by adsorption on activated carbon: Investigation of the thermal effects during the charging process*, *International Journal of Hydrogen Energy*. 32 (2007) 1542–1553. <https://doi.org/10.1016/j.ijhydene.2006.10.048>.
- [10] J. Xiao, L. Tong, C. Deng, P. Bénard, R. Chahine, *Simulation of heat and mass transfer in activated carbon tank for hydrogen storage*, *International Journal of Hydrogen Energy*. 35 (2010) 8106–8116. <https://doi.org/10.1016/j.ijhydene.2010.01.021>.
- [11] J. Xiao, J. Wang, D. Cossement, P. Bénard, R. Chahine, *Finite element model for charge and discharge cycle of activated carbon hydrogen storage*, *International Journal of Hydrogen Energy*. 37 (2012) 802–810. <https://doi.org/10.1016/j.ijhydene.2011.04.055>.
- [12] J. Xiao, L. Tong, D. Cossement, P. Bénard, R. Chahine, *CFD simulation for charge-discharge cycle of cryo-adsorptive hydrogen storage on activated carbon*, *International Journal of Hydrogen Energy*. 37 (2012) 12893–12904. <https://doi.org/10.1016/j.ijhydene.2012.05.079>.
- [13] A. Chakraborty, S. Kumar, *Thermal management and desorption modeling of a cryo-adsorbent hydrogen storage system*, *International Journal of Hydrogen Energy*. 38 (2013) 3973–3986. <https://doi.org/10.1016/j.ijhydene.2012.11.113>.
- [14] N. Cherrad, D. Selloum, S. Tingry, *Modeling the control of the desorption rate of hydrogen released from the adsorption storage bed to supply a fuel cell*, *International Journal of Hydrogen Energy*. 45 (2020) 17605–17612. <https://doi.org/10.1016/j.ijhydene.2020.04.120>.

- [15] G. Sdanghi, S. Schaefer, G. Maranzana, A. Celzard, V. Fierro, Application of the modified Dubinin-Astakhov equation for a better understanding of high-pressure hydrogen adsorption, *Applied Materials and Interfaces*. (n.d.) (Submitted).
- [16] J. Xiao, R. Peng, D. Cossement, P. Bénard, R. Chahine, CFD model for charge and discharge cycle of adsorptive hydrogen storage on activated carbon, *International Journal of Hydrogen Energy*. 38 (2013) 1450–1459. <https://doi.org/10.1016/j.ijhydene.2012.10.119>.
- [17] A. Delahaye, A. Aoufi, A. Gicquel, I. Pentchev, Improvement of hydrogen storage by adsorption using 2-D modeling of heat effects, *AIChE J.* 48 (2002) 2061–2073. <https://doi.org/10.1002/aic.690480919>.
- [18] R.B. Bird, W.E. Stewart, E.N. Lightfoot, *Transport Phenomena*, John Wiley & Sons, 2006.
- [19] J.W. Leachman, B. Jacobson, S. Penoncello, E.W. Lemmon, Fundamental Equations of State for Parahydrogen, Normal Hydrogen, and Orthohydrogen, 38 (2009) 721–748.
- [20] R.W. Powers, R.W. Mattox, H.L. Johnston, Thermal Conductivity of Condensed Gases. II. The Thermal Conductivities of Liquid Normal and of Liquid Parahydrogen from 15 to 27 K, *Journal of the American Chemical Society*. 76 (1954) 5972–5973.
- [21] K. Nasrifar, Comparative study of eleven equations of state in predicting the thermodynamic properties of hydrogen, *International Journal of Hydrogen Energy*. 35 (2010) 3802–3811. <https://doi.org/10.1016/j.ijhydene.2010.01.032>.
- [22] M.-A. Richard, P. Benard, R. Chahine, Gas adsorption process in activated carbon over a wide temperature range above the critical point. Part 1: modified Dubinin-Astakhov model, *Adsorpt.-J. Int. Adsorpt. Soc.* 15 (2009) 43–51. <https://doi.org/10.1007/s10450-009-9149-x>.
- [23] R.K. Ahluwalia, T.Q. Hua, J.-K. Peng, S. Lasher, K. McKenney, J. Sinha, M. Gardiner, Technical assessment of cryo-compressed hydrogen storage tank systems for automotive applications, *International Journal of Hydrogen Energy*. 35 (2010) 4171–4184. <https://doi.org/10.1016/j.ijhydene.2010.02.074>.
- [24] P. Bénard, R. Chahine, Determination of the Adsorption Isotherms of Hydrogen on Activated Carbons above the Critical Temperature of the Adsorbate over Wide Temperature and Pressure Ranges, *Langmuir*. 17 (2001) 1950–1955. <https://doi.org/10.1021/la001381x>.
- [25] M.-A. Richard, P. Benard, R. Chahine, Gas adsorption process in activated carbon over a wide temperature range above the critical point. Part 2: conservation of mass and energy, *Adsorpt.-J. Int. Adsorpt. Soc.* 15 (2009) 53–63. <https://doi.org/10.1007/s10450-009-9150-4>.
- [26] M.M. Dubinin, Fundamentals of the theory of adsorption in micropores of carbon adsorbents: Characteristics of their adsorption properties and microporous structures, *Carbon*. 27 (1989) 457–467. [https://doi.org/10.1016/0008-6223\(89\)90078-X](https://doi.org/10.1016/0008-6223(89)90078-X).
- [27] D.D. Do, H.D. Do, Adsorption of supercritical fluids in non-porous and porous carbons: analysis of adsorbed phase volume and density, *Carbon*. 41 (2003) 1777–1791. [https://doi.org/10.1016/S0008-6223\(03\)00152-0](https://doi.org/10.1016/S0008-6223(03)00152-0).
- [28] F.P. Incropera, D.P. DeWitt, *Fundamentals of Heat and Mass Transfer*, 4th ed., Wiley, New York, USA, 1996.
- [29] A. Unterstell, 1.4980 (Alloy A-286), S66286 | Datasheet | METALCOR, (n.d.). <http://www.metalcor.de/en/datenblatt/78/> (accessed June 11, 2019).
- [30] R.H. Perry, D.W. Green, *Perry's Chemical Engineers' Handbook*, McGraw-Hill Professional, 1999. [http://125.234.102.150:8080/dspace/handle/DNULIB\\_52011/5086](http://125.234.102.150:8080/dspace/handle/DNULIB_52011/5086) (accessed February 27, 2017).
- [31] D. Durette, P. Bénard, R. Zacharia, R. Chahine, Investigation of the hydrogen adsorbed density inside the pores of MOF-5 from path integral grand canonical Monte Carlo at

supercritical and subcritical temperature, *Science Bulletin*. (2016). <http://agris.fao.org/agris-search/search.do?recordID=US201700096435> (accessed January 24, 2019).

- [32] G. Sdanghi, R. Canevesi, A. Celzard, M. Thommes, V. Fierro, Characterization of Carbon Materials for Hydrogen Storage and Compression, *Journal of Carbon Research*. 6 (2020) 46. <https://doi.org/10.3390/c6030046>.
- [33] M.V. Lototsky, V.A. Yartys, B.G. Pollet, R.C. Bowman, Metal hydride hydrogen compressors: A review, *International Journal of Hydrogen Energy*. 39 (2014) 5818–5851. <https://doi.org/10.1016/j.ijhydene.2014.01.158>.
- [34] P. Ramirez-Vidal, G. Sdanghi, A. Celzard, V. Fierro, High hydrogen release by cryo-adsorption and compression on porous materials, *International Journal of Hydrogen Energy*. 47 (2022) 8892–8915. <https://doi.org/10.1016/j.ijhydene.2021.12.235>.

# Supplementary information



SI 1 : Comparison between the specific heat capacities of bulk hydrogen (normal hydrogen) obtained from the NIST database (colored full lines) and from the models proposed for the temperature ranges of: (a) 77-175 K and (b) 175 – 450 K (models in black dashed lines), and (c) and (d) residuals of the two models (compared to NIST values) for the same temperature ranges of (a) and(b), respectively.

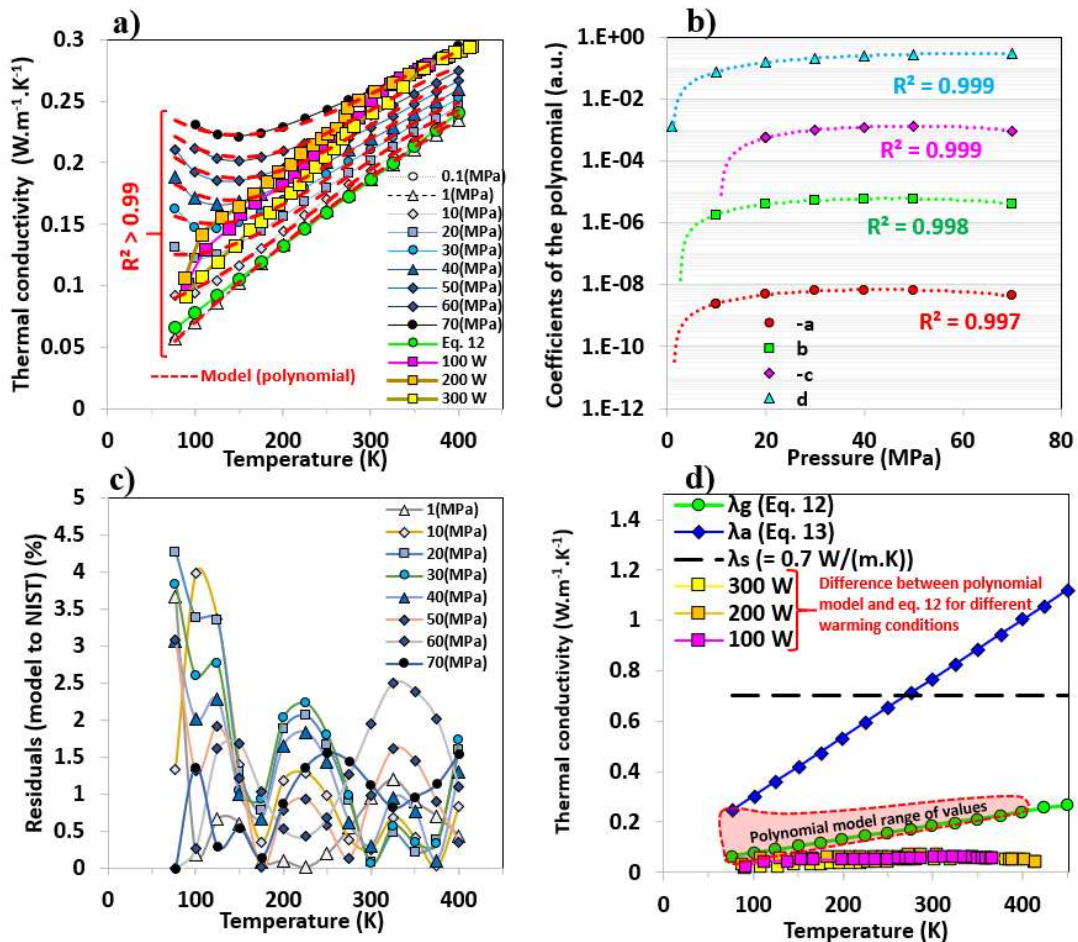
**Calculation note:** In order to obtain an explicit expression of the thermal conductivity of the hydrogen bulk phase ( $\lambda_g$ ) depending on pressure and temperature, a polynomial regression was carried out on a set of points obtained using the REFPROP-8® software (NIST database):

$$\lambda_g = a(P).T(K)^3 + b(P).T(K)^2 + c(P).T(K) + d(P)$$

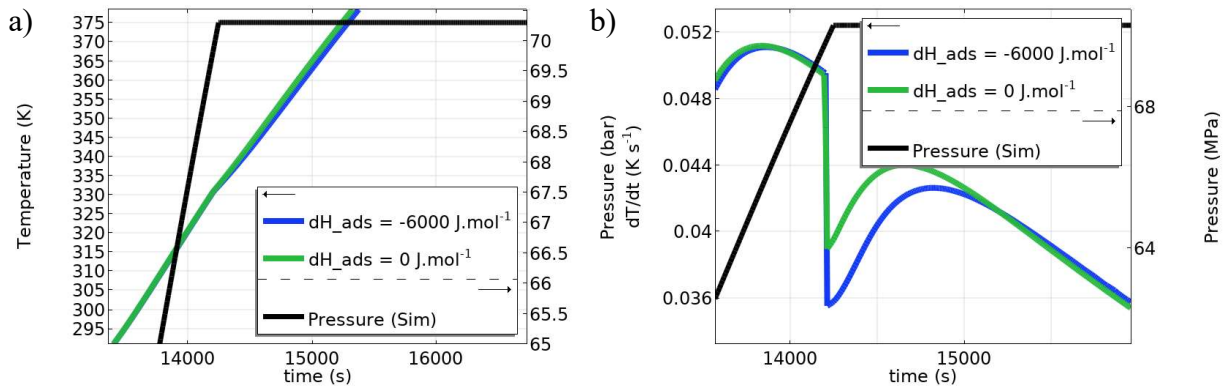
where each coefficient ( $a$ ,  $b$ ,  $c$  and  $d$ ) depends on pressure. The quality of each regression was assessed by observing the  $R^2$  value ( $R^2 > 0.99$ ). The result of such regression can be observed in Figure SI 2. a) (red dashed lines). The difference between the as-modelled values and NIST ones can be observed in Figure SI 2. c). The difference between the values obtained using the polynomial model and the NIST values, within the 0.1 – 70 MPa and 77-400 K pressure and temperature ranges, was less than 5% (Figure SI 2. c)). The expression used to model the pressure dependence of each coefficient ( $a$ ,  $b$ ,  $c$  and  $d$ ) was also a polynomial.

$$\chi = \alpha.P(\text{MPa})^2 + \beta.P(\text{MPa}) + \gamma$$

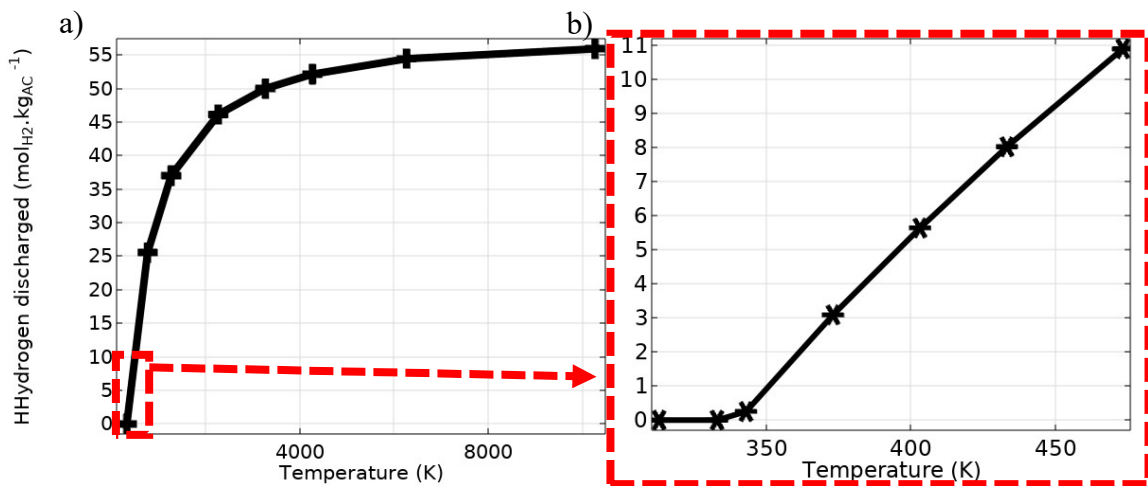
where  $\chi$  corresponds to a coefficient ( $a$ ,  $b$ ,  $c$  or  $d$ ).  $\alpha$ ,  $\beta$  and  $\gamma$  are the pressure-dependence coefficients.  $\alpha$ ,  $\beta$  and  $\gamma$  values differ depending on the chosen coefficient ( $a$ ,  $b$ ,  $c$  and  $d$ ). The quality of the regression, obtained for each coefficient, can be observed in Figure SI 2. b).



SI 2 : NIST values of bulk hydrogen thermal conductivity ( $\lambda_g$ ) depending both on pressure and temperature, and its polynomial fit: (a) values obtained for the experiments according to fitting and to Eq. 12 ; (b) pressure dependence of the polynomial coefficients; (c) residuals of the polynomial fitting (compared to NIST values); and (d) comparison between thermal conductivities of hydrogen bulk and adsorbed phases ( $\lambda_g$ ,  $\lambda_a$ ) and porous carbon ( $\lambda_s$ ), and difference between Eq. 12 and polynomial model values obtained using experimental data points (P, T).



SI 3 : Impact of the heat of adsorption: (a) on the temperature; and (b) on the temperature derivative -  $dT / dt$ .



SI 4 : (a) Total amount of hydrogen discharged per kg of activated carbon as a function of set point temperature; (b) area zoomed up to 473.15 K.